Speed-Dependent Alignment and Angular Distributions of $O(^1D_2)$from the Ultraviolet Photodissociation of N_2O

David W. Neyer, Albert J. R. Heck,† and David W. Chandler*

Combustion Research Facility, Sandia National Laboratories, Livermore, California 94551, and Departments of Chemistry and Pharmacy, Utrecht Univeristy, Utrecht, The Netherlands

Janne M. Teule‡ and Maurice H. M. Janssen

Laser Centre and Chemistry Department, Vrije Universiteit, Amsterdam, The Netherlands

Received: July 2, 1999; In Final Form: September 23, 1999

Photofragment ion imaging has been used to study the $O(^1D_2)$ atoms produced in the ultraviolet (~200 nm) photodissociation of nitrous oxide (N_2O) in a molecular beam. The images of $O(^1D_2)$ reveal a speed-dependent angular distribution resulting from both variation in the spatial anisotropy of the recoil and alignment of the electronic angular momentum of the $O(^1D_2)$ fragment. The orbital alignment effects are revealed by a change in the images when different transitions of the O atom are employed in the resonance enhanced multiphoton ionization (REMPI) process. By correlating the O atom anisotropies with previously measured values for the complementary N_2 fragments and comparing images collected on two different REMPI transitions, we calculate the relative branching ratios and anisotropies for the three different $|m|$ values (defined along the product recoil axis) of the electronic angular momentum of the $O(^1D_2)$ fragment. While $m = 0$ fragments have the highest probability for most O atom speeds, there is a significant change in the alignment and angular distributions for the slower O atoms. We use a simplified dynamical model supported by previous theoretical structure calculations to explain the measured trends and to estimate the relative branching in the excitation to two N_2O electronic states.

1. Introduction

Because of its importance in atmospheric chemistry, the photophysics of nitrous oxide, N_2O, has been the subject of considerable study.[1−5] The ultraviolet photodissociation of N_2O in the stratosphere is a primary source of excited $O(^1D_2)$ atoms which react with other N_2O molecules to produce NO. These NO radicals play a principal role in the catalytic destruction of ozone. Furthermore, N_2O is one of the important greenhouse gases and the global budget of nitrous oxide in the atmosphere has been under much debate over the past few years.[6] The photolysis of N_2O has also been implicated in the isotope enrichment of the stratosphere.[7−9] In addition to its atmospheric importance, the photodissociation of N_2O is an important source of electronically excited oxygen atoms for labortory studies of chemical kinetics and dynamics.[10−12] N_2O is relatively easy to handle in a laboratory setting, and its ultraviolet photodissociation around 200 nm produces little or no ground-state $O(^3P)$ atoms that would complicate experimental measurements. Also, the N_2 cofragment is relatively inert in most chemical systems.

Many higher pressure kinetics experiments require only knowledge of the product branching in the photodissociation and possibly the average translational energy of the $O(^1D_2)$ atoms. However, detailed theoretical and experimental reaction dynamics investigations would benefit greatly from a more complete characterization of the $O(^1D_2)$ reactant. For instance, recent experiments studying stereodynamics of $O(^1D_2)$ reactions require a knowledge of the correlated speed and angular distribution of the $O(^1D_2)$ reactant as well as any orbital alignment effects.[10−12] Because of its permanent dipole and the symmetric top behavior of the molecule with bending excitation, N_2O can be rotationally state selected and oriented using hexapole focusing and electric fields.[13,14] These characteristics open many possibilities for studying reactions in which a reactive $O(^1D_2)$ atom can be pointed at another reactant or surface by orienting its N_2O precursor. However, the additional detail that can be revealed from such experiments also requires an exacting description of the photodissociation process.

Not only is an accurate and quantitative description of the photodissociation process and of the characteristics of the resulting O atom products necessary for the understanding of further experiments, it is also important for understanding the electronic potential surfaces and dynamics of N_2O and for testing theoretical methods and predictions. N_2O provides an important and tractable system for studying the shapes and couplings of excited potential energy surfaces in a small molecule.[15,16] Our experiments use the ion imaging technique with velocity mapping to measure the translational energy distribution of the $O(^1D_2)$ atom. Using the polarization of the laser light and studying multiple REMPI transitions, we also determine the alignment of the $O(^1D_2)$ fragment.

The first measurements of the angular and speed distribution for a triatomic unimolecular dissociation were conducted by Busch and Wilson in 1972 on the NO_2 and NOCl molecules.[17] Due to their long time-of-flight distance, the speed resolution they obtained in 1972 was better than that we can obtain with our apparatus. We, however, have a laser ionization source (instead of electron bombardment) that allows us to selectively

† Departments of Chemistry and Pharmacy.
‡ Present address: Art Innovation bv Holland, Westermaatsweg 11, 7556 BW Hengelo, The Netherlands.

10.1021/jp9922918 CCC: $18.00
Published on Web 11/18/1999

detect products populating a single rovibrational quantum state and thereby greatly simplifying the translational energy spectrum. The laser's polarization also allows us to determine the alignment of the products. Furthermore, modern imaging techniques record the projected two-dimensional recoil velocity distribution providing a multiplex detection advantage. The translational spectroscopy technique applied in Busch and Wilson's seminal work can be regarded as the ancestor of the present ion-imaging technique.

A number of experimental studies have been aimed at determining the velocity distribution of the $O(^1D_2)$ product from N_2O photodissociation. Experiments conducted by Felder et al.[1] indicated that the $O(^1D_2)$ velocity distribution produced in the 193 nm photodissociation of N_2O could be characterized by an anisotropy parameter,[18] β, of 0.48 and that approximately 42% of the available energy was found in the translational energy of the fragments. At approximately the same time, a study by Shafer et al.[3] using Doppler-resolved resonance enhanced multiphoton ionization time-of-flight mass spectrometry (REMPI-TOFMS) of the $O(^1D_2)$ atom concluded that nearly all of the available energy was released in translational motion and that the angular distribution was best described by $\beta = 2$. A pair of later experiments were in better agreement with the conclusions of Felder et al.[1] Springsteen et al.[4] used Doppler-resolved LIF in the vacuum ultraviolet to detect the $O(^1D_2)$ atom. By making measurements with combinations of photodissociation and detection polarizations, and assuming a single β parameter for all speeds of the O atom, they determined that the translational energy E_{trans} was equal to 42% of the available energy E_{avail} and that $\beta = 0.50$. Hanisco and Kummel[2] measured the N_2 energy distribution directly using REMPI-TOFMS and determined that 40−56% of E_{avail} was found in translation. They also used TOF techniques to examine the angular distribution, but could only conclude that the β value was positive.

These experiments provide a good estimate for the translational energy distribution and the average β parameter that describe the photodissociation. However, the ion imaging experiments of Suzuki et al.[5] and of our own group[19] reveal even more complexity. Suzuki et al. measured the ion image of the $O(^1D_2)$ fragment in a one-laser experiment using 205.8 nm light. The laser dissociated the N_2O parent and ionized the $O(^1D_2)$ through a two-photon ($^1P_1 - ^1D_2$) REMPI transition. From the image, they concluded that there were two components to the dissociation process: one with a broad translational energy distribution (ranging from 0 to 60 kcal/mol) and a low value of β and the other with a more narrow translational energy distribution peaked at ~25 kcal/mol and with a higher β value. These two components produce a translational energy distribution that appears to have a main peak with tails at both lower and higher translational energies. They also determined that the β parameter increases from 0 to 1 as the translational energy increases from 0 to 26 kcal/mol and then fell back down to lower β values for higher translational energies. Suzuki et al. also state that there was some indication of orbital alignment in the $O(^1D_2)$ image.

In our imaging studies[19] of the N_2 fragment after photolysis of N_2O at ~203 nm, we found that the β parameter was approximately one for N_2 fragments with $J < 50$ and that it slowly decreased to approximately 0.7 for N_2 ($J = 74$). The β value then fell dramatically to approximately zero for the highest N_2 rotational levels detected ($J \sim 90$). This was determined by recording an image for each individual rotational state of the N_2 fragment. Because the N_2 fragment and the O atom are coupled by conservation of momentum, this change in β parameter observed in the N_2 fragment must also be present in the O atom. Measuring the angular distibutions via the N_2 fragment is more reliable than using the $O(^1D_2)$ image because the Q-branch (2+1)REMPI transition used is not very sensitive to alignment of the N_2 rotational angular momentum and each state can be spectrally resolved and therefore measured separately.[20,21]

As Suzuki et al. state, the $O(^1D_2)$ images are affected by alignment of the $O(^1D_2)$ electronic angular momentum. Since the imaging technique allows us to determine the full three-dimensional distribution of ions, we can study the angular distribution and alignment for each velocity component of the $O(^1D_2)$ atom. Because there is the possibility of excitation of two excited states leading to the same product states in the dissociation, coherent interferences can affect the angular distributions of the fragments.[22−24] However, since we are probably exciting N_2O from both the ground state and vibrationally excited states[25] and the $O(^1D_2)$ products correlate with many different ro-vibrational states of the N_2 fragment, each having a different angular distribution which we do not fully resolve, we have not included coherence effects in our analysis. Attempts to measure coherences in this dissociation process have recently been reported using 193 nm photolysis.[26]

In this paper we present images of $O(^1D_2)$ from N_2O photodissociation taken on three different two-photon resonant REMPI transitions probing the $O(^1D_2)$. By combining these data with the angular distributions determined from the N_2 images, we are able to determine the speed-dependent populations and angular distributions of the magnetic sublevels $|m|$ of the aligned O atom defined along the product recoil axis. In part 2 we describe briefly the experimental setup used. In part 3 we present the experimental results and the data analysis of the measured images. In part 4 we discuss the alignment observed and relate this to a simplified qualitative model of the electronic orbitals involved in the excitation and dissociation. From this analysis we estimate the product state dependent branching ratio between the $1^1A''(^1\Sigma^-)$ and $2^1A'(^1\Delta)$ excited states of N_2O. In part 5 we present our conclusions.

2. Experimental Section

The experimental apparatus and procedures for data collection and analysis have been described previously,[27−30] and the specific methods used for these experiments are nearly identical to those used for the N_2 images.[19] Briefly, a molecular beam of neat N_2O is expanded into a vacuum chamber and through a small collimating hole in the repeller plate of an ion optics setup. The molecular beam is crossed by a laser with a wavelength between 198 and 206 nm which both dissociates the N_2O parent and ionizes the $O(^1D_2)$ product. For most experiments, the UV light is generated by frequency tripling the output of a Nd:YAG pumped dye laser. The laser is scanned over the Doppler profile of the $O(^1D_2)$ REMPI transitions while the images are collected. For two-laser experiments a second UV laser pulse is generated at 205.8 nm by sum frequency mixing the ~488 nm output of a dye laser or optical parametric oscillator with the 355 nm third harmonic of a Nd:YAG laser. The ionized oxygen atoms are accelerated into a field free TOF tube and detected with a position-sensitive detector consisting of a pair of microchannel plates and a phosphor screen. The light from the phosphor is recorded with a cooled CCD camera.

Two different ion optics arrangments are used in these experiments.[19] In the initial experiments the conventional setup, which consists of a flat, fine mesh extraction grid to accelerate the ions, is used. This method allows us to calibrate the size of

the image and therefore to determine the velocity of the O atom fragments. This ion optics arrangement directly projects the ions onto the imaging detector without magnification. By measuring the arrival time and the image size a velocity distribution is directly measured. However, the spatial extent of the overlap between the dissociation laser and the molecular beam creates a line source of ions which blurs the image.[31]

A second ion optic arrangement, velocity mapping,[31−33] is also used for the O images taken at 203.5 and 205.8 nm. This arrangement increases the resolution of the image by eliminating the blurring caused by the finite volume of the overlap between the molecular beam and the focused laser. By replacing the extraction grid with an electrostatic lens setup, like that described by Eppink and Parker,[31,32] we are able to focus this line source to a point at the detector and remove much of the blurring from our images. The resulting images are in fact a velocity map of the fragment ions and are typically magnified in size by approximately 15%.[33] In the experiment, the extraction grid is replaced by a middle extraction ring and ground ring approximately 12 mm apart with circular aperatures of approximately 25 mm and 18 mm diameter, respectively. The last plate is grounded, while the middle plate is adjusted in voltage to create the best focusing (typically ∼70% of the repeller voltage).

The experiments are performed at a 50-Hz repetition rate. The camera is controlled by, and images are collected on, an Apple Macintosh (Quadra 700) computer. Further processing of the images, including the use of the inverse Abel transform[34] to reconstruct the three-dimensional velocity distributions from the two-dimensional projections, is conducted on a UNIX based workstation (Silicon Graphics Indigo^2) and a Macintosh Quadra 630.

3. Experimental Results and Data Analysis

3.1. Experimental Results. As shown in Figure 1, images are collected in which one laser beam is used for both dissociation and REMPI light for the ionization of the O($^1D_2$) product at 198.5, 203.5, and 205.8 nm corresponding to two-photon transitions in the O atom from the $^1D_2$ state to the $^1D_2$, $^1F_3$, or $^1P_1$ states, respectively.[35] The images at 203.5 and 205.8 nm were collected with both the flat mesh extraction technique and with the higher resolution of the velocity map ion lens setup. The higher resolution of the velocity map technique can be seen by comparing the flat field image of Figure 1a with the images in Figure 1b and c. Additionally, the slight top/bottom asymmetry of the images, due to nonuniformity in the response of the detector, is less severe in Figure 1b and c which used a better detector. This slight variation has a small effect on the angular distributions, and therefore, both halves of the images are used in the data analysis and fitting procedures.

The significant differences in the images taken at the three wavelengths, see Figure 1, which are probing the same product photodissociation, indicate the presence of orbital alignment in the O($^1D_2$) fragment. Two color experiments were also conducted by dissociating at 205.8 nm and probing at 203.5 nm and vice versa. These experiments reveal that the difference in these images is in fact due to the REMPI probe transition and not to changes in the dynamics between these two photolysis energies.

As discussed in our previous study[19] of the N_2 fragments, the use of a neat beam of N_2O did not lead to any apparent problems with cluster formation. The N_2 rotational distributions with neat N_2O are consistent with those measured by Hanisco and Kummel[2] under a variety of expansion conditions. However, the vibrationally warmer beam generated is expected to increase the relative contribution of excitation from vibrationally excited parent N_2O molecules.

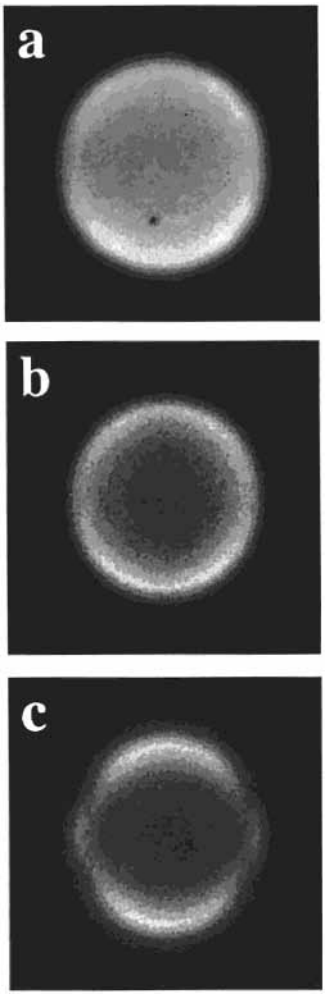

Figure 1. Photofragment ion images of O($^1D_2$) produced in the photodissociation of N_2O. The images are each collected with one laser wavelength near 200 nm which is used for both dissociation and resonant ionization of the O atom products. The wavelengths and associated two-photon transition in the REMPI scheme are (a) 198.5 nm, $^1D_2-^1D_2$; (b) 203.5 nm, $^1F_3-^1D_2$; and (c) 205.8 nm, $^1P_1-^1D_2$. The differences in the images are due to the electronic orbital alignment of the O($^1D_2$) product and the relative detection efficiency of the alignment for each transition. Image (a) is taken with flat ion optics (and therefore has a different size on the detector) while (b) and (c) are collected with the velocity map ion optics. Only (b) and (c) were used in the data analysis.

The raw images, which are two-dimensional projections of the three-dimensional O^+ ion distribution, are inverted using an inverse Abel transform to create an intensity profile through the true three-dimensional velocity distribution. This procedure can be used when the image contains an axis of cylindrical symmetry. Because of the orbital alignment, the O atom images can only be directly inverted when the polarization of both the dissociation and probe lasers are parallel and in the plane of the detector. It should be noted that the transform gives an intensity profile through the three-dimensional (3D) velocity distribution of the ions. However, the ion distribution is a convolution of the 3D velocity distribution of the O($^1D_2$) neutral fragments and the ionization cross-section of the REMPI transition (which has an angular dependence that depends on the orbital alignment).

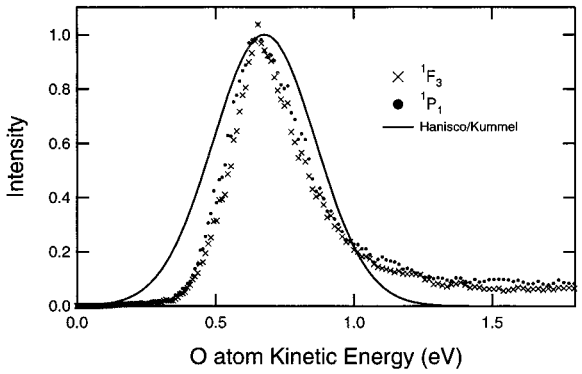

Figure 2. Integrated kinetic energy distributions of the $O(^1D_2)$ fragments determined from the images shown in Figure 1b and c for the $^1F_3-^1D_2$ (●) and $^1P_1-^1D_2$ (×) transitions. The solid line is the Gaussian distribution determined from the N_2 REMPI experiments of Hanisco and Kummel (ref 2).

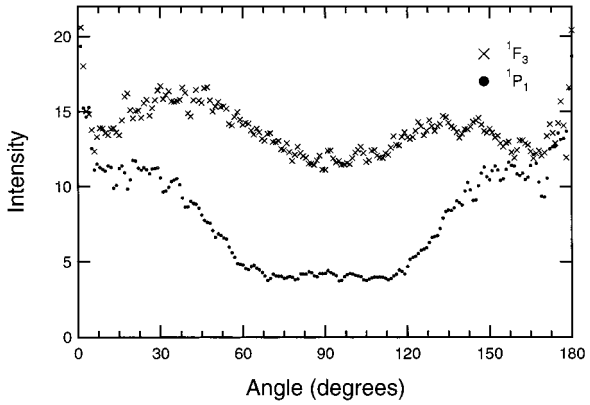

Figure 3. Angular distributions of $O(^1D_2)$ fragment ions detected in Figure 1b and c integrated over all speeds. The data are for the $^1F_3-^1D_2$ (●) and $^1P_1-^1D_2$ (×) transitions.

The kinetic energy distribution of the O atoms can be calculated by integrating the transformed profile over all angles and converting from velocity to kinetic energy. This distribution is shown in Figure 2. Because of the orbital alignment and the angular dependence of the ionization cross-section for the $O(^1D_2)$, the calculated intensities in the distribution are not rigorously accurate. However, the kinetic energy distributions (shown in Figure 2) calculated using both the 203.5 nm and the 205.8 nm transitions, which have dramatically different angular dependence, produce nearly identical distributions indicating they are accurate representations of the true distribution. These distributions are also consistent with the measurements of Hanisco and Kummel.[2] From their measurements of the N_2 rotational distribution and translational energies, Hanisco and Kummel were able to calculate a kinetic energy distribution for the $O(^1D_2)$ fragments. This Gaussian fit to the kinetic energy distribution is also presented in Figure 2. The peak of the distribution matches quite well with our imaging measurements.

The angular distribution of $O(^1D_2)$ ions can also be calculated from the inverse Abel transformed profile. The total angular distribution (shown in Figure 3) is calculated by integrating over all speeds. The transform process leads to some accumulation of noise along the symmetry axis of the inverted image, at 0 and 180 degrees in the angular plots. Additionally, one can calculate the angular distribution integrated over a much more narrow range of speeds (radii in the image). The angular distributions shown in Figure 4 are for rings which are 10 pixels wide at selected radii of the $^1P_1$ and $^1F_3$ images collected with the velocity map technique. The corresponding O atom velocity

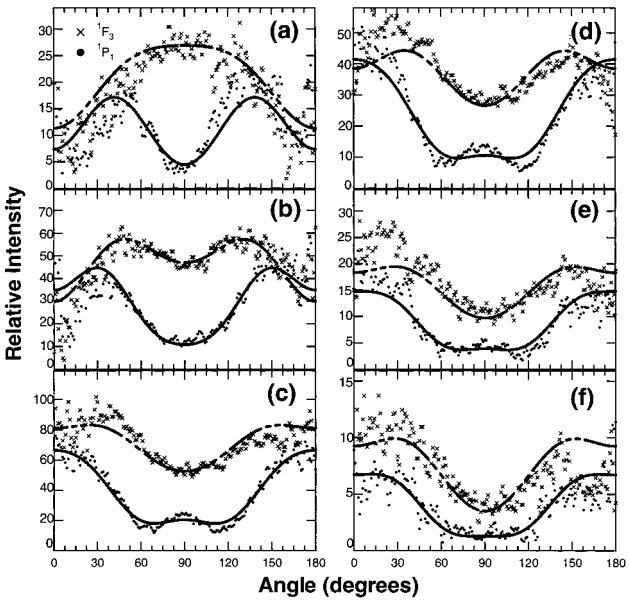

Figure 4. Angular distributions of $O(^1D_2)$ fragment ions detected in Figure 1b and c for selected ranges of radii (O atom velocities). The data points are for the $^1F_3-^1D_2$ (●) and $^1P_1-^1D_2$ (×) transitions and the solid and dashed lines, respectively, represent the least-squares fit (described in the text) to the data. The corresponding O atom velocities, N_2 rotational levels, and parameters of the fit are given in Table 1. The radii ranges are: (a) 90−100 pixels, (b) 100−110, (c) 110−120, (d) 120−130, (e) 130−140, and (f) 140−150.

ranges and N_2 cofragment rotational quantum numbers are indicated in Table 1.

As clearly shown in Figure 4, the measured angular distributions of the ions change dramatically as the velocity of the O atom changes. These differences are due to changes in the angular recoil distribution of the neutral atoms (as reflected in the N_2 angular distribution) and changes in the orbital alignment (as reflected in the angular dependence of the ionization probability). For the angular distributions presented in Figure 4, the recoil distribution of neutral atoms is the same. However, because of the orbital alignment, the measured ion distributions for the two REMPI transitions are quite different. These differences are due to the changes in the angular dependence of the REMPI cross sections for the $^1P_1$ and $^1F_3$ transitions. From our measurements of the N_2 images and determination of the rotationally specific β values we have determined the overall angular distribution of the neutral O atoms in a given ring (speed). By using this information, which is true for a given speed in either transition, along with the angular dependence of the ionization cross-section we can determine the orbital alignment of the $O(^1D_2)$ for each ring of a given speed.

3.2. Data Analysis. For a given O atom speed, the detected ion distribution I_{image} is a product of the neutral recoil distribution I_{rec} and the REMPI detection efficiency I_{det}:

$$I_{image} \propto I_{rec} \times I_{det} \tag{1}$$

As described previously, the recoil distribution is given by[18]

$$I_{rec} \propto 1 + \beta P_2(\cos\theta) \tag{2}$$

where θ is the angle between the polarization axis of the photolysis light and the recoil velocity, P_2 is the second-order Legendre polynomial, and β is the anisotropy parameter. The detection efficiency I_{det} for the two-photon transition depends on the angular momentum distribution of the fragment. Since the excited states either autoionize at the two-photon level or

TABLE 1: The Relative Populations and β Values for the $|m|$ Sublevels of $O(^1D_2)$ Fit to the Angular Distributions for the Selected Ranges of Radii Shown in Figure 4[a]

pixel range	average velocity (km/s)	$J(N_2)$	$\beta(N_2)$	fit	populations $m=0$	populations $\|m\|=1$	populations $\|m\|=2$	β values $m=0$	β values $\|m\|=1$	β values $\|m\|=2$	χ^2
90−100	2.34	80−83	0.16	LS	0.64	0.23	0.13	0.14	0.16	0.25	8.22
				E	0.75	0.20	0.05	0.2	0.0	0.2	
100−110	2.59	75−79	0.68	LS	0.54	0.42	0.04	0.89	0.39	0.91	4.04
				E	0.57	0.38	0.05	1.1	0.0	1.1	
110−120	2.83	70−74	0.83	LS	0.21	0.71	0.08	2.0	0.35	2.0	1.40
				E	0.30	0.63	0.07	2.0	0.2	2.0	
120−130	3.08	64−69	0.93	LS	0.26	0.70	0.04	2.0	0.48	2.0	2.96
				E	0.32	0.63	0.05	2.0	0.3	2.0	
130−140	3.33	56−63	1.0	LS	0.27	0.64	0.09	2.0	0.46	1.98	4.64
				E	0.25	0.70	0.05	2.0	0.6	2.0	
140−150	3.57	48−55	1.2	LS	0.33	0.57	0.10	2.0	0.69	1.67	4.05
				E	0.30	0.60	0.10	2.0	0.7	2.0	

[a] The table also correlates these ranges with the corresponding O atom velocities and N_2 fragment rotational levels. The parameters for both the linear least-squares fit (LS) and a fit "by eye" (E) (as described in the text) are presented.

easily absorb a third photon (saturated), the angular dependence of the two-photon transition should accurately describe the ionization cross section. Following the theory presented by Kummel et al.[36] for determining the angular momentum distribution of species probed by a two-photon process, we calculate the detection efficiencies for a set of magnetic sublevels, m, of the $J = 2$ electronic orbital angular momentum of the $O(^1D_2)$ fragments.

Since the chemical significance of the orbital alignment is best described in the molecular frame, we define a quantization axis along the velocity vector of the dissociating fragments, and assume that the angular momentum distribution is cylindrically symmetric about this axis.[37] Because we only employ a single, linearly polarized laser for photolysis and detection, we only determine the population of the fragments in $|m| = 0$, 1, and 2. With these simplifications, we can write

$$I_{\mathrm{det}} \propto \sum_k Q_k(J_i,J_f) c_k A_0^{(k)}(J_i) P_k(\cos\theta) \tag{3}$$

where P_k are Legendre polynomials, c_k are normalization factors, and $k = 0$, 2, and 4. $A_0^{(k)}(J)$ are spherical tensor components of the alignment of angular momentum J. Using the proportionality constants $c(k)$ given in Kummel et al.,[36] and expanding in the populations p_m of the magnetic sublevels,

$$A_0^{(k)}(J) = \frac{c(k)\langle J||J^{(k)}||J\rangle}{[J(J+1)]^{k/2}} \sum_m p_m (-1)^{J-m} \begin{pmatrix} J & \mathrm{k} & J \\ -m & 0 & m \end{pmatrix} \tag{4}$$

The Q_k in eq 3 are the line strength factors for fragments recoiling along the direction of the polarization of the laser as given by Mo et al.[37] For the $^1F_3-^1D_2$ and $^1P_1-^1D_2$ transitions in the O atom (where $J_f \neq J_i$), we can calculate the line strength factors without explicit knowledge about the one-photon virtual states. This is not possible for the $^1D_2-^1D_2$ transition ($J_f = J_i$) at 198.5 nm without further knowledge of the component transition moments. Normalizing Q_4c_4 and Q_2c_2 by Q_0c_0, we can transform eq 3 into

$$I_{\mathrm{det}} \propto 1 + a_2 A_0^{(2)} P_2(\cos\theta) + a_4 A_0^{(4)} P_4(\cos\theta) \tag{5}$$

where

$$a_2 = -5\sqrt{\frac{5}{21}}(-1)^{J_f+J_i} \frac{J_i(J_i+1)(2J_i+1)}{\langle J_i||J_i^{(2)}||J\rangle} \begin{Bmatrix} J_i & J_i & 2 \\ 2 & 2 & J_f \end{Bmatrix}$$

$$a_4 = \frac{36}{7}(-1)^{J_f+J_i} \frac{(2J_i+1)[J_i(J_i+1)]^2}{\langle J_i||J_i^{(4)}||J_i\rangle} \begin{Bmatrix} J_i & J_i & 4 \\ 2 & 2 & J_f \end{Bmatrix} \tag{6}$$

Using eq 6 we determine that $a_2 = 0.8163$ and $a_4 = -0.7347$ for the $^1F_3-^1D_2$ transition while $a_2 = -0.7143$ and $a_4 = -6.857$ for the $^1P_1-^1D_2$ transition.

To determine the $|m|$ dependence of the detection efficiency, we calculate the $A_0^{(k)}$ values for each of the three $|m|$ levels (shown in Table 2) and use eq 5 to calculate the angular dependence of I_{det}. Plots of I_{det} for the three $|m|$ levels are shown in Figure 5 for both the $^1F_3-^1D_2$ and $^1P_1-^1D_2$ two-photon transitions. It is immediately obvious from the significant differences between Figure 5a and b that alignment of the O atom angular momentum can produce very different angular distributions of detected ions. It is also interesting to note that for the $^1P_1-^1D_2$ transition, only $|m| = 1$ is ionized along the laser polarization (0° and 180°), while both $|m| = 1$ and 2 contribute at these angles for the $^1F_3-^1D_2$ transition.

We analyze the data as if each of the three $|m|$ sublevels is an independent dissociation product. Initial analysis of the alignment of the O atom was conducted by assuming the angular distribution, described by the β parameter, for all $|m|$ levels was equal to that determined from the corresponding N_2 images:

$$I_{\mathrm{rec}} \propto [1 + \beta P_2(\cos\theta)] \sum_m p_m I_{\mathrm{det}}(m) \tag{7}$$

By varying the three $|m|$ level populations, we tried to fit the angular distributions for both the $^1P_1$ and $^1F_3$ REMPI transitions. This method was not successful in adequately fitting the data. For some velocities the angular distributions could not be reasonably fit by varying only the population of the $|m|$ components with all $|m|$ having a single fixed value of β (a three parameter fit to all the data sets). The data were therefore fit using independent β values for each of the three $|m|$ populations (a six parameter fit to the data set):

$$I_{\mathrm{rec}} \propto \sum_m p_m [1 + \beta_m P_2(\cos\theta)] I_{\mathrm{det}}(m) \tag{8}$$

These parameters were constrained both by the ability to fit the intensity distributions at all angles for both O atom transitions for a given radius and by the need to match the overall β value (given by the sum of each $|m|$ level population times its $|m|$-dependent β value) to that of the corresponding N_2 images. In addition, the overall scaling ratio between the two O atom images had to be maintained for all speeds. This

TABLE 2: Alignment Moments Calculated for an Angular Momentum Distribution with $J = 2$ and All Populations in a Single $|m|$ Level

$\|m\|$	$A^{(2)}_{0,m}$	$A^{(4)}_{0,m}$
0	−1.0	0.25
1	−0.5	−0.1667
2	1.0	0.0417

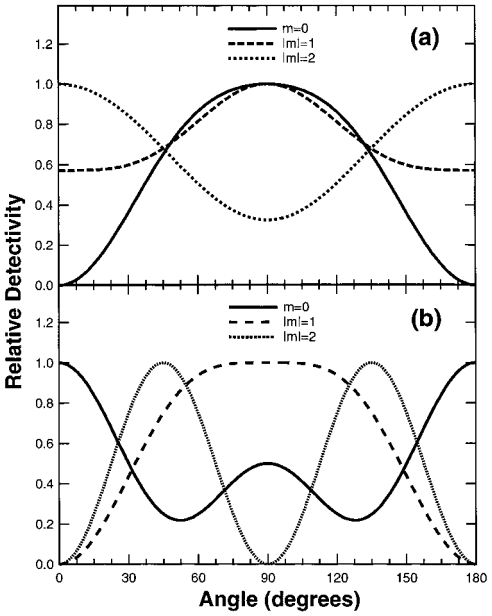

Figure 5. Plots of the angular dependence of the ionization cross-section for different $|m|$ levels (—, $m = 0$; − − −, $|m| = 1$; and ···, $|m| = 2$) of $O(^1D_2)$ (as described in the text). The plots are for the two transitions (a)$^1F_3 - ^1D_2$ and (b)$^1P_1 - ^1D_2$ and reveal the high sensitivity to orbital alignment for an isotropic angular distribution ($\beta = 0$) of fragment velocities.

leaves only four independent parameters to be fitted. Even with these constraints, the additional degrees of freedom for fitting greatly increased the uncertainties in the fits. As will be discussed, the idea of independent β values for each $|m|$ level is not unreasonable when multiple electronic transitions and excited potential energy surfaces are involved in the dynamics.

The fits were conducted using two methods. The first was to vary the parameters interactively and to qualitatively judge the goodness of fit (fitting by eye). This method helps reveal specific constraints on the system and allows one to discern the main trends in the data. The second method employed was a linear least-squares fitting program subject to the constraints of the system. This method provides an unbiased, quantitative fit to the data. The results of the computed fit are in remarkably good agreement with the fit by eye. The results of both fitting methods are presented in Table 1 with relative χ^2 values for the least-squares fit. The results from the least-squares fitting are used in the other plots and for further analysis. While the error on the fits for some of the parameters are fairly large (e.g., the value of β for $|m| = 2$ has a high uncertainty due to its small population), some very specific trends and bounds on these populations and β values are apparent.

The populations of the three different $|m|$ levels for each speed ring from the least-squares fit are shown in Figure 6 and the corresponding β values are presented in Figure 7. The data are plotted versus rotational level of the N_2 cofragment and O atom velocity (or radius of the image). Very little population is found in the $|m| = 2$ level for any translational energy, and as the rotation in the corresponding N_2 fragment increases, the predominant $|m| = 1$ population decreases while the $m = 0$ population increases. Because the $|m| = 2$ population is so small, there is a very large uncertainty in its β value. For most of the fits, its value is nearly equal to the β of $m = 0$. While the β value for $m = 0$ decreases sharply for the highest rotational levels of N_2, the $|m| = 1$ β is found to remain near zero throughout the data range.

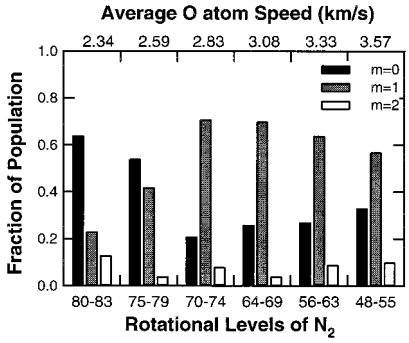

Figure 6. Plot of the $|m|$ level populations (tabulated in Table 2) of $O(^1D_2)$ as a function of the N_2 cofragment rotational levels and O atom velocity calculated with a least-squares fit to the angular distributions in Figure 4.

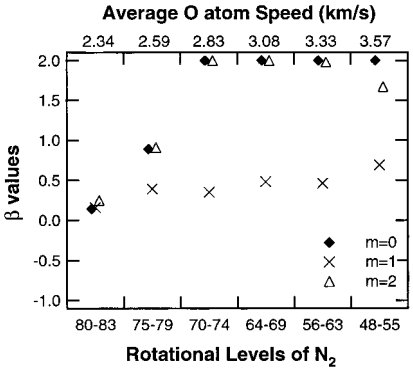

Figure 7. Plot of the β_m values (tabulated in Table 2) for the$|m|$ levels of $O(^1D_2)$ as a function of the N_2 cofragment rotational levels and O atom velocity calculated with a least-squares fit to the angular distributions in Figure 4.

4. Discussion

Although the ultraviolet photodissociation of the small triatomic molecule N_2O may appear to be a fairly simple dynamical process at first glance, these imaging experiments reveal a much more complex situation. The detail with which we can examine this dissociation and characterize the resulting fragments allows us to reveal the true complexity of the dynamics in this "simple" system. By coupling the results from images of the N_2 fragments with the data presented here, we are able to not only characterize the $O(^1D_2)$ velocity and alignment but to learn about the potential energy surfaces and dynamics responsible for it.

The translational energy distribution of the O atom fragments is a particularly important parameter in reaction dynamics studies which use these hot atoms as reactants. The total translational energy distributions determined from our images are shown in Figure 2. As stated in the results section, these direct calculations of the distributions are not rigorous because of the alignment in the O atom product. However, the fact that both REMPI transitions (which have very different alignment detectivities) give essentially identical distributions imply that these are fairly accurate descriptions. These distributions are also consistent with the internal energy distributions of the N_2 fragment (and the calculated $O(^1D_2)$ kinetic energy distribution) determined by

Hanisco and Kummel[2] and confirmed in our own work.[19] They are, however, different from the distribution published by Suzuki et al.,[5] for low translational energies. Suzuki et al. observe a significant low energy tail to the distribution and attribute these lower energy O atoms to a second dissociation channel. We note that the distributions presented in Figure 2 are determined from images taken with the velocity map ion-optics arrangement. The absolute velocity scale of these images is calibrated with the flat field ion optics images. The velocity map images have little or no broadening along the laser propagation direction. In our own images taken with the conventional flat field optics, a slight increase in the low energy part of the translational energy distribution is also observed.

The angular distribution and alignment of the O atoms from this photodissociation are experimentally entwined, but by comparing the images taken from two O atom REMPI transitions and using the data from our N_2 images, we have been able to determine trends in both the $|m|$ level populations and the anisotropy parameters for each of those $|m|$ levels. While the information presented in Figures 6 and 7 appears somewhat complex at first, it can in fact be explained in a fairly straightforward way by examining the possible electronic transitions along with the corresponding potential energy surfaces and crossings responsible for dissociation. We have based much of our analysis on the theoretical calculations for these excited states published by Hopper.[15]

From Hopper's calculations (and shown in Figure 8) we see that the first two excited singlet states of N_2O are the $1^1A''(^1\Sigma^-)$ and the $2^1A'(^1\Delta)$ states. While the $2^1A'(^1\Delta)$ state is part of a Renner−Teller pair, the other component of this pair has a linear equilibrium geometry and its energy increases rapidly as the molecule bends. Since the excitation transition in N_2O is enhanced through vibronic coupling caused by bending,[25] this higher energy state is unlikely to play a role in this photodissociation. A closer examination of the transitions to and dynamics on the $1^1A''$ and $2^1A'$ state potential energy surfaces reveals both important similarities and differences.

In the reduced C_s symmetry of a bent N_2O molecule, the transition dipole for excitation from the $1^1A'(^1\Sigma^+)$ ground electronic state to the $1^1A''$ $(^1\Sigma^-)$ excited state is out-of-plane. In contrast, the transition dipole for excitation to the $2^1A'(^1\Delta)$ state will lie in the plane of the bent N_2O and nearly parallel to the N−O bond for small bending angles. For the prompt dissociation expected on either of these two surfaces, these differences in the transition dipole directions will lead to differences in the anisotropy parameters expected for the dissociation products.[19] The out-of-plane (or perpendicular) transition will produce a $\beta = -1$ anisotropy parameter even if the N_2O parent undergoes significant bending motion before dissociation. The in-plane transition to the $2^1A'$ state is expected to be nearly parallel for small bending angles of the N_2O parent and would result in a value of $\beta = 2$. However, if the parent molecule bends before dissociation, the fragment velocity vector will no longer be as highly aligned with the transition dipole (and therefore the polarization of the dissociation laser) and the value of β will be reduced.[17] The resulting β value can be described by the expression $\beta = \beta_{max}P_2(\cos\alpha)$, where $\beta_{max} = 2$, P_2 is the second-order Legendre polynomial, and β is the bending angle.

While the transition dipoles to the two excited states are different, the general topologies of the two potential energy surfaces appear to be quite similar. According to Hopper's calculations, both states are strongly bent, with equilibrium bending angles near 130° (see Figure 8a). The difference in

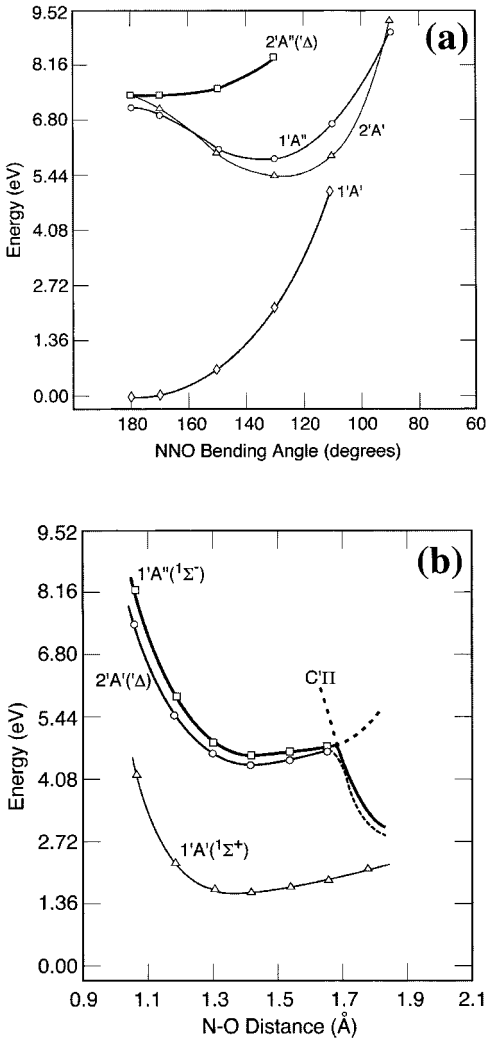

Figure 8. Representations of potential energy curves for the electronic states of N_2O involved in the UV photodissociation. The curves in (a) show the dependence of the potential on the bending coordinate of N_2O (with a fixed N−O distance), while (b) shows the crossing of two excited states by the dissociative $^1\Pi$ state at longer N−O bond distances (for a fixed bending angle of ∼130°). Curves adapted from ref 15.

energy between the linear N_2O molecule and this minimum in the bending angle is approximately 1.5 eV which corresponds very well with the average amount of energy deposited in N_2 fragment rotation. An additional similarity between these two electronic states is that they become dissociative by undergoing an avoided crossing with the repulsive $^1\Pi$ state (see Figure 8b). For angles near the minimum of the bending potential, this crossing takes place at very similar R(O−N_2) distances (approximately 1.7 Å). The crossings from the $2^1A'(^1\Delta)$ and $1^1A''(^1\Sigma^-)$ states to the $^1\Pi$ state (or more specifically its A′ and A″ components) are responsible for dissociation of these excited states and provide considerable insight into the dynamics which determine both the $|m|$ level populations and the corresponding β values.

Hopper provides molecular orbital descriptions of each of these states in the linear and bent symmetries along with the contribution of the oxygen atom's 2p electrons (or holes) to each of these molecular orbitals.[38] Both the linear $^1\Delta$ and the $^1\Sigma^-$ molecular states can be assigned the $2\pi^3 3\pi$ electron configuration, while the $^1\Pi$ state is $2\pi^3 7\sigma_A$. When the linear C_{2v} symmetry is reduced to C_s by bending, the molecular orbitals are characterized simply by a′ and a″. The three electronic states involved differ only by the occupation of two orbitals. For the

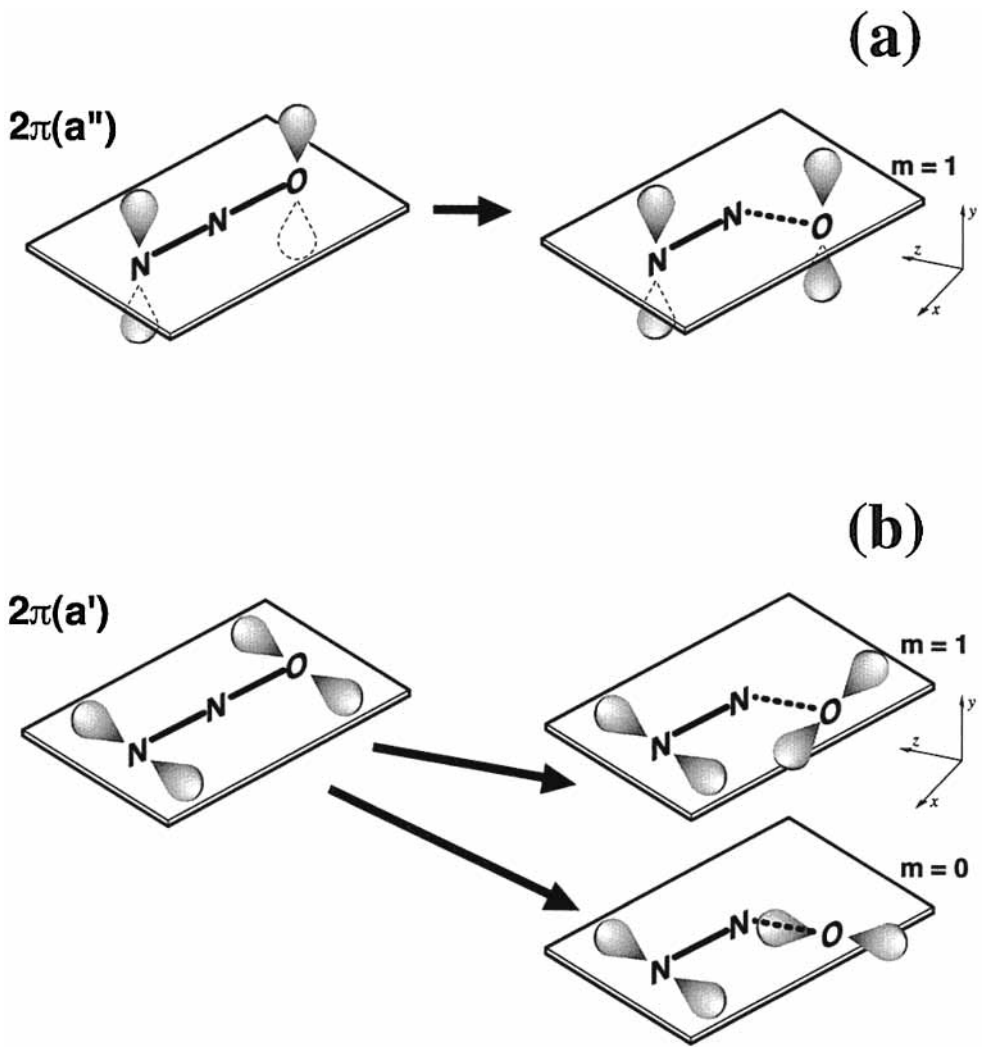

Figure 9. Schematic representation of the evolution of the 2π molecular orbital of N_2O upon bending during dissociation. In (a) the orbital has a″ symmetry upon bending (corresponding to dissociation of the $1^1A''(^1\Sigma^-)$ state) and produces an O atom with its p orbital out of the plane of bending (y-axis) yielding $|m| = 1$. In (b) the orbital has a′ symmetry (corresponding to dissociation of the $2^1A'(^1\Delta)$ state) and can produce an O atom p orbital aligned either along the dissociation vector (z-axis) giving $m = 0$ or perpendicular to the dissociation vector (x-axis) giving $|m| = 1$.

$2^1A'(^1\Delta)$ state, one of the 2π orbitals correlates with a 9a′, while the 3π orbital correlates with 10a′. For the $1^1A''(^1\Sigma^-)$ state, the correlation is $2\pi \rightarrow 2a''$ and $3\pi \rightarrow 10a'$, and for the $^1\Pi$ state, $2\pi \rightarrow 9a'$ and $7\sigma_A \rightarrow 8a'$.

Since the N_2 resulting from this dissociation of N_2O is produced in the symmetric ground $^1\Sigma^+$ electronic state, it is the $O(^1D_2)$ atom which retains the electronic angular momentum. The $O(^1D_2)$ state has a $1s^22s^22p^4$ electron configuration and so it is the 2p electrons (or the corresponding 2p holes) that account for the angular momentum. We therefore look at the 2p contributions to each of the molecular orbitals. From Hopper's calculations we find that the 3π molecular orbital has a significant contribution from the O atom 2p electron with an antibonding N−O π contribution. The 2π orbital has much of its electron density localized as an O(2p) electron with the rest localized on the N atom at the opposite end of the molecule.

If we examine the evolution of these orbitals (and, in particular, the O atom 2p contribution to them) during the dissociation process, we can get an initial understanding of the orbital alignment effects. We define a coordinate system with the z-axis along the velocity vector of the dissociating fragments, the x-axis in the bending plane of the triatomic at a right angle to the z-axis, and the y-axis perpendicular to this plane (see Figure 9). The p orbitals from the O atom can be defined along these axes and give corresponding contributions to the $|m|$ sublevels defined on the z-axis. The p_z orbital has a zero projection along the velocity vector, while the p_x and p_y orbitals are linear combinations of the orbitals with $m = \pm 1$. Using these axes we now examine the evolution of the p orbitals that contribute to the relevant molecular orbitals of the N_2O molecule.

For both the $2^1A'(^1\Delta)$ and $1^1A''(^1\Sigma^-)$ states, the 3π orbital in the linear configuration has a′ symmetry upon bending. Near the linear configuration, this corresponds to having the O atom p electron in a p_x orbital. In contrast, the dissociative $^1\Pi$ state has its O atom p electron in the p_z orbital corresponding to a dissociative, antibonding sigma orbital. If we assume that the dissociative electronic surface is dominated by this "σ-type" bonding with the electron in a p_z orbital as the molecule bends, we can infer the coupling that leads to dissociation. As the N_2O parent bends, the p_x orbital of the $^1\Delta$ and $^1\Sigma^-$ states can couple to the p_z orbital since they both have a′ symmetry. This coupling, which can be expected to be reasonably large due to the electron density on the adjacent N atom in the 3π orbital, is therefore the coupling to the Π state and leads to prompt dissociation. As a result, one p electron on the O atom is occupying a p_z orbital. By treating the N_2O π orbitals independently, we see that the 3π orbital makes a $m = 0$ contribution to the overall

atomic orbital alignment. Therefore, the magnetic sublevel populations of the O atom are limited to population in $|m| = 0$ and 1 and the relative populations are determined by the p electron from the 2π orbital. This conclusion is consistent with the measured alignments in which very little population is found in the $|m| = 2$ component.

The p electron contribution to the 2π orbital of N_2O can be treated similarly, but with very different results (see Figure 9). For the $1A''$ state, the O atom p electron in this orbital is p_y (with a$''$ symmetry), while for the $2A'$ state, it is p_x (with a$'$ symmetry). Because the p_y orbital does not couple with the p_x and p_z orbitals of a$'$ symmetry, this electron remains p_y during dissociation and provides an $|m| = 1$ contribution to the alignment (see Figure 9a). Therefore by combining the $m = 0$ contribution of the 3π orbital with the $|m| = 1$ contribution of the 2π orbital, we conclude that dissociation on the $1^1A''$ surface only yields $|m| = 1$ O atom products. In contrast, the $2^1A'$ state has a p_x orbital which can remain as p_x (with $|m| = 1$) or couple with the p_z orbital ($m = 0$) when the N_2O parent bends (see Figure 9b). The overall alignment from dissociation on the $2^1A'$ surface can therefore have both $m = 0$ and $|m| = 1$ contributions.

According to Hopper's calculations, the 2π orbital can be characterized by an O atom p electron separated from the rest of the electron density which is found on the far N atom. It is not surprising, therefore, that the electron in this O atom p orbital does not feel large perturbations, particularly for small bending angles. One would therefore expect that dissociation at small bending angles on the $2^1A'$ surface are characterized by the electron remaining in a p_x orbital and an overall O atom population in $|m| = 1$. As the molecule bends during dissociation (leading to higher J levels of N_2), one could expect more coupling between the p_x and p_z orbitals and an increase in the population of $m = 0$ from the $2^1A'$ state (see Figure 9b). As noted above, the $1^1A''$ state only gives $|m| = 1$.

As we discussed previously, the overall β parameter for the dissociation (as measured in the N_2 fragment) is determined by the percentage of the excitation going to the $2^1A'$ and $1^1A''$ surfaces and the corresponding β parameters for dissociation on those surfaces. From our discussions, we estimate that the O atom fragments with $m = 0$ reveal the β parameter for the bending $2^1A'$ surface, while the $1^1A''$ surface maintains a β of -1 even after bending (assuming no rotation). Therefore, the β parameter for the O atom fragments with $|m| = 1$ is an average of these two β values weighted by the relative A$'$ and A$''$ contributions and can be used to calculate the ratio of the dissociation channels. Using this simple model (and attributing the small $|m| = 2$ contribution to the $2^1A'$ state) we can calculate the overall ratio of $2^1A'$ to $1^1A''$ dissociation as a function of the O atom speed or N_2 rotational level (shown in Figure 10). We estimate that between 20 and 40% of the dissociation takes place on the $1^1A''(^1\Sigma^-)$ surface for all but the highest J levels of N_2 (corresponding to the highest bending of the parent). For these high J fragments, the dissociation occurs almost completely on the $2^1A'(^1\Delta)$ surface. However, the overall β parameter for these fragments is greatly reduced due to bending in the N_2O parent.[19] Overall, these measurements of the velocity-dependent angular distributions and orbital alignments, the calculated $|m|$-dependent populations and β values, and the inferred branching between the electronic surfaces should provide high level tests of future potential energy surfaces and dynamics calculations for this system.

5. Conclusions

We have used ion imaging to make detailed measurements of the $O(^1D_2)$ fragment from the photodissociation of N_2O. By measuring images for a pair of two-photon probe transitions of the O atom, and coupling these data with imaging measurements of the N_2 fragments, we have been able to make speed-resolved determinations of the O atom alignment and angular distribution. We find little population in $|m| = 2$ for all of the O atom speeds, and while $|m| = 1$ is the most populated state for most of the distribution, $m = 0$ is the most probable for the slowest O atom fragments (corresponding with high J levels of N_2). The $|m|$ level distributions have been explained using a molecular orbital model based on calculations of the excited electronic surfaces by Hopper. This model allows us to calculate the $|m|$ level populations and β values and to estimate, as a function of the O atom speed, the branching between the $2^1A'$ and $1^1A''$ electronic states excited in the process. These studies reveal the complexity occurring in the photodissociation dynamics of this small molecule. The imaging technique has provided details that have either been previously unresolved in experiments on this molecule or have led to incomplete analysis. The calculations of Hopper have been instrumental in understanding the observed dynamical trends, and hopefully these experimental results will lead to further advanced dynamics calculations on the surfaces calculated by Hopper or new calculated potentials.

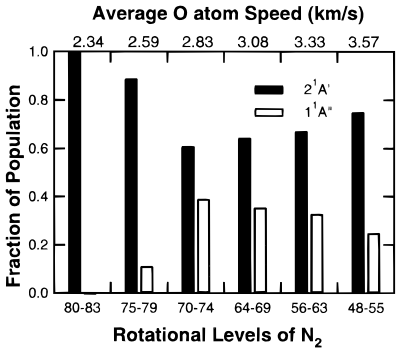

Figure 10. Plot of the estimated relative branching ratio for excitation to the $2^1A'(^1\Delta)$ and $1^1A''(^1\Sigma^-)$ excited electronic states of N_2O as a function of the N_2 cofragment rotational levels and fragment O atom velocity. The calculated branching is based on the $|m|$-dependent populations and β values (see text for details).

Acknowledgment. This research has been funded by the U.S. Department of Energy, Office of Basic Energy Sciences, Division of Chemical Sciences. The authors thank Mr. W. G. Roeterdink for help on the two-laser photolysis experiments and discussions, Dr. C. A. Taatjes and Dr. G. C. Groenenboom for helpful discussions, and Prof. S. Stolte for support and discussions.

References and Notes

(1) Felder, P.; Haas, B.-M.; Huber, J. R. *Chem. Phys. Lett.* **1991**, *186*, 177.
(2) Hanisco, T. F.; Kummel, A. C. *J. Phys. Chem.* **1993**, *97*, 7242.
(3) Shafer, N.; Tonokura, K.; Matsumi, Y.; Tasaki, S.; Kawasaki, M. *J. Chem. Phys.* **1991**, *95*, 6218.
(4) Springsteen, L. L.; Satyapal, S.; Matsumi, Y.; Dobeck, L. M.; Houston, P. L. *J. Phys. Chem.* **1993**, *97*, 7239.
(5) Suzuki, T.; Katayanagi, H.; Mo, Y.; Tonokura, K. *Chem. Phys. Lett.* **1996**, *256*, 90.
(6) Rahn, T.; Zhang, H.; Wahlen, M.; Blake, G. A. *Geophys. Res. Lett.* **1998**, *25*, 4489.
(7) Cliff, S. S.; Thiemens, M. H. *Science* **1997**, *278*, 1774.
(8) Rahn, T.; Wahlen, M. *Science* **1997**, *278*, 1776.
(9) Yung, Y. L.; Miller, C. E. *Science* **1997**, *278*, 1778.
(10) Alexander, A. J.; Aoiz, F. J.; Brouard, M.; Burak, I.; Fujimura, Y.; Short, J.; Simons, J. P. *Chem. Phys. Lett.* **1996**, *262*, 589.
(11) Brouard, M.; Duxon, S. P.; Enriquez, P. A.; Simons, J. P. *J. Chem. Phys.* **1992**, *97*, 7414.

(12) Brouard, M.; Lambert, H. M.; Short, J.; Simons, J. P. *J. Phys. Chem.* **1995**, *99*, 13571.
(13) Teule, J. M.; Neyer, D. W.; Chandler, D. W.; Janssen, M. H. M. Ion-imaging of the photodissociation of state-selected N_2O. In preparation.
(14) Teule, J. M. Dynamical aspects of alkaline earth metal reactions and the photon-induced dissociation of nitrous oxide, Ph.D. Thesis, Vrije Universiteit, 1997.
(15) Hopper, D. G. *J. Chem. Phys.* **1984**, *80*, 4290.
(16) Janssen, M. H. M.; Teule, J. M.; Stolte, S.; Neyer, D. W.; Chandler, D. W.; Groenenboom, G. C. In *Molecular Beams*; Campargue, R., Ed.; Springer-Verlag: New York, 1999. In press.
(17) Busch, G. E.; Wilson, K. R. *J. Chem. Phys.* **1972**, *56*, 3638.
(18) Zare, R. N. *Mol. Photochem.* **1972**, *4*, 1.
(19) Neyer, D. W.; Heck, A. J. R.; Chandler, D. W. *J. Chem. Phys.* **1999**, *110*, 3411.
(20) Hanisco, T. F.; Kummel, A. C. *J. Phys. Chem.* **1991**, *95*, 8565.
(21) Hanisco, T. F.; Yan, C.; Kummel, A. C. *J. Phys. Chem.* **1992**, *96*, 2982.
(22) Bracker, A. S.; Wouters, E. R.; Suits, A. G.; Vasyutinski, O. S. *J. Chem. Phys.* **1999**, *110*, 6749.
(23) Rakitizis, T. P.; Zare, R. N. *J. Chem. Phys.* **1999**, *110*, 3341.
(24) Suzuki, T.; Katayanagi, H.; Nanbu, S.; Aoyagi, M. *J. Chem. Phys.* **1998**, *109*, 5778.
(25) Selwyn, G. S.; Johnston, H. S. *J. Chem. Phys.* **1981**, *74*, 3791.
(26) Ahmed, M.; Wouters, E. R.; Peterka, D. S.; Vasyutinskii, O. S.; Suits, A. G. *Faraday Discuss.* **1999**, *113*, 425.
(27) Heck, A. J. R.; Chandler, D. W. *Annu. Rev. Phys. Chem.* **1995**, *46*, 335.
(28) Chandler, D. W.; Houston, P. L. *J. Chem. Phys.* **1987**, *87*, 1445.
(29) Kitsopoulos, T. N.; Buntine, M. A.; Baldwin, D. P.; Zare, R. N.; Chandler, D. W. *SPIE Proc.* **1993**, *1858*, 2.
(30) Thoman, J. W.; Chandler, D. W.; Parker, D. H.; Janssen, M. H. M. *Laser Chem.* **1988**, *9*, 27.
(31) Eppink, A. T. J. B.; Parker, D. H. *Rev. Sci. Instrum.* **1997**, *68*, 3477.
(32) Parker, D. H.; Eppink, A. T. J. B. *J. Chem. Phys.* **1997**, *107*, 2357.
(33) Parker, D. H.; Chandler, D. W. *Adv. Photochem.* **1999**, *25*, 56.
(34) Smith, L. M.; Keefer, D. R.; Sudharsanan, S. I. *J. Quant. Spectrosc. Radiat. Transfer* **1988**, *39*, 367.
(35) Pratt, S. T.; Dehmer, P. M.; Dehmer, J. L. *Phys. Rev. A* **1991**, *43*, 4702.
(36) Kummel, A. C.; Sitz, G. O.; Zare, R. N. *J. Chem. Phys.* **1986**, *85*, 6874.
(37) Mo, Y.; Katayanagi, H.; Heavan, M. C.; Suzuki, T. *Phys. Rev. Lett.* **1996**, *77*, 830.
(38) Hopper, D. G. Physics Auxiliary Publication Service Document No. JCPSA-80-4290-100. American Institute of Physics: Woodbury, NY.